

A Novel Asymmetric Interior Permanent Magnet Synchronous Machine

Y. Xiao, *Member, IEEE*, Z.Q. Zhu, *Fellow, IEEE*, G. W. Jewell, J. T. Chen, D. Wu, and L.M. Gong

Abstract—This paper proposes a novel asymmetric interior permanent magnet (AIPM) rotor topology that has a mixed V-shape and spoke-type PM configuration, designated as a 1.5-layer PM structure, and asymmetric arrangement of V-shape PMs and asymmetric flux barriers. The AIPM rotor topology is employed for IPM synchronous machines to utilize the magnetic-field-shifting (MFS) effect for increasing average torque by reducing the current angle difference between peak PM and reluctance torque components. Three machines, i.e. the proposed 1.5-layer AIPM, a symmetrical 1.5-layer IPM-I and a conventional V-shape benchmark IPM-II are designed and optimized using the same stator, rotor diameter and total PM usage by global parametric optimization considering the mechanical stress. The effect of asymmetric features of the 1.5-layer AIPM rotor design, i.e. asymmetry of V-shape cavity as well as position and dimensions of flux barrier, on maximum torque and open-circuit air-gap field are investigated. The electromagnetic performances of three machines are compared. It confirms that the proposed AIPM machine has the highest maximum torque and the smallest cogging torque simultaneously. It is also revealed that the torque enhancement is achieved by both the 1.5-layer structure and MFS effect. Finally, a prototype of AIPM machine is manufactured and tested to validate the analyses.

Index Terms—Asymmetric rotor, interior permanent magnet (IPM), magnetic-field-shifting (MFS), reluctance torque, spoke-type PM

I. INTRODUCTION

INTERIOR permanent magnet (IPM) machines are preferable in many industrial applications due to their predominant performances including high power density, wide constant power speed range (CPSR) and desirable mechanical strength especially for high speed operation [1]. Besides, utilization of reluctance torque in IPM machines can reduce the usage of unsustainable and expensive rare-earth PM material to ease both resource and cost issues [2].

As rotor topologies in IPM machines, featured by PM configuration and rotor core geometry including the design of PM cavity, flux barrier and iron rib, are crucial for machine performance, many IPM rotor structures have been reported in literature and applied in industry [3, 4]. Among them, single layer structures, including spoke-type, V- and flat-shape IPMs, and double layer Delta-shape design are the most popular topologies due to their good performance and easy manufacturability. These topologies, as well as a U-shape

structure, are designed for electric vehicle application and their electromagnetic performances are compared in [4], while the comparison between the V-shape, U-shape, flat-shape and mixed V- and U-shape topologies are reported in [5]. Both comparisons indicate that machines using V-shape design can produce the highest torque density. In [6], a Y-shape rotor topology that combines V-shape and spoke-type PMs is proposed for fractional-slot concentrated winding IPM machines. The Y-shape IPM machine shows the highest torque density and the smallest torque ripple using the 12-slot/10-pole configuration compared with the conventional V-shape and spoke-type counterparts. Torque density enhancement without more PM usage remains an attractive topic for novel IPM rotor topology to improve both the machine performance and the utilization of PM material. To achieve this goal, multi-layer rotor structures have been widely studied for increasing reluctance torque due to high saliency. IPM machines with single-, double-, three-, six- and ten-layer circular PMs are compared in [7]. It shows significant enhancement of maximum torque when the number of PM layer increase from one to two and indicates that the largest rotor saliency is achieved by the triple-layer design. The comparison between IPM machines with V-shape, Delta-shape, double flat-shape and mixed Delta- and U-shape rotor topologies is reported in [8] and [9]. It is found that the highest torque density and highest efficiency are achieved by Delta-shape and mixed Delta- and U-shape designs, respectively. To mitigate the usage of rare-earth material, researchers are also interested in using low-cost PM material in multi-layer IPM machines, such as ferrite and Al-Ni-Co. PM-assisted synchronous reluctance machines with ferrite PMs are proposed in [10]–[12] for high torque density applications. In [13], a multi-layer IPM machine using Al-Ni-Co PMs is proposed, which shows improvements of torque density, power factor and torque ripple, compared with a synchronous reluctance machine. Nevertheless, complicated structure with many pieces of PMs in multi-layer IPM rotor topologies usually results in time-consuming design optimization and concerns for manufacturing and PM assembly issues.

Existing IPM machines with symmetrical rotor topologies have inherent current angle difference between maximum PM and reluctance torque components that is typically 45 electrical degrees (Elec. deg.), which consequently reduces the utilization ratios of both torque components in the maximum resultant

Y. Xiao, Z. Q. Zhu and G. Jewell are with Department of Electronic and Electrical Engineering, University of Sheffield, Sheffield, S1 3JD, U.K. (e-mail: yang.xiao@ieee.org, z.q.zhu@sheffield.ac.uk, g.jewell@sheffield.ac.uk).

J. T. Chen, D. Wu and L. M. Gong are with the Midea Shanghai Motors and Drives Research Center, Shanghai, China (e-mail: chenjintao@welling.com.cn, wudi9@welling.com.cn and gongliming@midea.com)

torque. Accordingly, a novel design concept is proposed by using asymmetric rotor structure to shift the peak points of PM and reluctance torque components to be closer, thereby increasing the average torque with the same PM usage, which is designated as magnetic-field-shifting (MFS) effect in literature. In [14] and [15], an IPM machine whose rotor exhibits poles using shifted inset PMs and V-shape PMs alternatively is proposed to utilize the MFS effect. [16] adds asymmetric flux barrier in a V-shape IPM, which shows a clear increase of average torque. Extra flux barrier is employed in the spoke-type IPM machine with non-overlapping winding in [17]. Compared with an existing AIPM machine using asymmetric rotor shaping and a conventional spoke-type IPM machine using the same stator and the same PMs, the proposed spoke-type AIPM machine shows significant torque enhancement and notable reduction of cogging torque and torque ripple simultaneously. [18] proposes a rotor design with symmetrical rotor geometry and asymmetric PM configuration that has significant torque enhancement compared with the symmetrical counterpart due to MFS effect, but the rotor structure is complicated. Another multi-layer AIPM rotor topology with symmetrical core structure and asymmetric PM configuration with inset PMs in q -axis is proposed in [19], which shows increase of average torque, reduction of torque ripple, and improvement of efficiency compared with a three-layer symmetrical IPM machine using inset d -axis PMs. [20] proposes a simple AIPM machine with asymmetric V-shape PMs and an additional outer flux barrier in each pole for electric vehicles. Compared with the conventional V-shape IPM machine benchmark in Toyota Prius 2010, the proposed AIPM machine shows significant torque enhancement due to utilizing MFS effect and better torque-speed characteristics. An AIPM machine topology using hybrid-layer PM configuration is introduced in [21] with significant torque enhancement and torque ripple suppression compared with the conventional V-shape IPM machine benchmark. The concept of MFS technique is also employed in a PM-assisted salient-pole wound rotor synchronous machine in [22] for enhancement of reluctance torque.

A novel asymmetric IPM (AIPM) rotor topology using the mixed V-shape and spoke-type PM configuration with asymmetric features including the angle shifting between axes of V-shape PMs and spoke-type PMs as well as the position and dimensions of extra flux barriers near the rotor surface is proposed in [23] for torque enhancement in IPM synchronous machine. The PM configuration is designated as the 1.5-layer PM structure because the spoke-type PM is defined as a half layer as it is shared by adjacent poles. The proposed 1.5-layer AIPM machine benefits from both the 1.5-layer design and asymmetric features, which can achieve simple multi-layer structure with only three pieces of PMs in each pole and utilize MFS effect, respectively, for significantly increasing torque density compared with the conventional V-shape IPM machine using the same stator, rotor diameter and total PM volume. In this paper which is an extension of [23], the concept of MFS technique is briefly indicated, and the design optimization is improved by employing mechanical stress analysis for iron

bridge design. The investigation of influences of asymmetric features in AIPM machine and the comparison of electromagnetic performances between three optimal machines are both extended. More advantages of the proposed AIPM machine, including the significant reduction of cogging torque and improvement of efficiency, are also revealed. Moreover, the AIPM machine prototype is manufactured and tested, and experimental results are provided for verification.

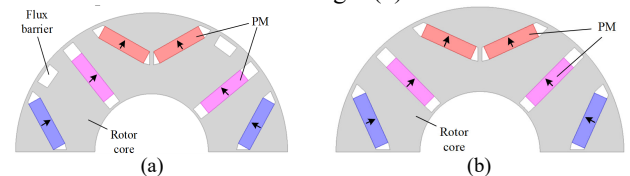
This paper is organized as follows: Section II describes the proposed asymmetric 1.5-layer mixed V-shape and spoke PM AIPM topology, Fig.1(a), the symmetrical 1.5-layer IPM topology, Fig.1(b), and the conventional V-shape IPM topology, Fig.1(c). The concept of MFS technique is also briefly introduced. Design optimization of three machines are presented in Section III with the same stator, rotor diameter and PM usage and mechanical stress characteristics are considered. The influence of asymmetric features in AIPM machine on maximum average torque and open-circuit air-gap flux density distribution is investigated in Section IV. In Section V, electromagnetic performances of the proposed AIPM and IPM-I machines are compared with the conventional IPM-II machine to reveal the merits and demerits of the proposed machine. The measured results of the AIPM prototype are provided in Section VI and the conclusion is given in Section VII.

II. PROPOSED MACHINE TOPOLOGY

A. Machine Topologies

The proposed novel AIPM rotor topology with an asymmetric 1.5-layer mixed V-shape and spoke PM configuration, as well as an extra asymmetric flux barrier near the rotor surface in each pole, is illustrated in Fig. 1 (a). Compared with the symmetrical IPM-I machine using 1.5-layer mixed V-shape and spoke PM configuration as shown in Fig. 1 (b), the asymmetry of AIPM machine can be observed as featured by angle shifting between axes of V-shape and spoke PMs and the asymmetric flux barrier near the rotor surface between the right-side V-shape and spoke-type PMs in each pole. It should be noted that both AIPM and IPM-I machine using the 1.5-layer PM configuration are firstly proposed in [23].

These features make both rotor geometry and PM configuration in AIPM machine exhibit asymmetric distribution and thus MFS effect for torque enhancement. Besides, a conventional V-shape IPM benchmark IPM-II is employed for comparison as shown in Fig. 1(c) that has the same stator, rotor diameter and total PM volume to both 1.5-layer IPM machines. Magnetization directions of PMs are denoted by arrows in Fig. 1. The same 24-slot/4-pole stator with single-layer integer-slot distributed windings applied for all three machines is illustrated in Fig. 1(d).



> REPLACE THIS LINE WITH YOUR PAPER IDENTIFICATION NUMBER (DOUBLE-CLICK HERE TO EDIT) <

3

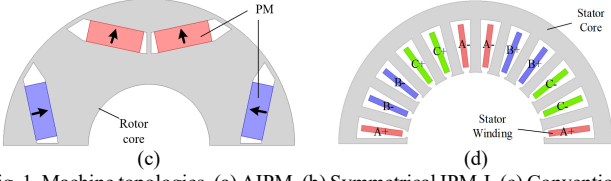


Fig. 1. Machine topologies. (a) AIPM. (b) Symmetrical IPM-I. (c) Conventional V-shape IPM-II. (d) Stator design.

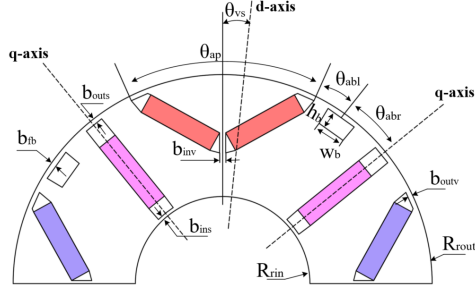


Fig. 2. Rotor geometric model and main design parameters of the proposed AIPM machine.

The rotor geometric model of the AIPM machine is shown in Fig. 2. The d -axis of the AIPM is located at the central axis between adjacent spoke PMs, while the q -axis remains at the conventional position that has a 90 Elec. deg. angle difference from the d -axis. The position of V-shape PMs is characterized by the angle between central axes of V-shape PMs and spoke PMs, namely θ_{vs} , in each pole, which indicates the asymmetry of V-shape PMs. The asymmetry factor β_{vs} is defined to describe the asymmetry of V-shape PMs in AIPM machine as

$$\beta_{vs} = 4p\theta_{vs} / \theta_{cir} \quad (1)$$

where p is the pole pair number and θ_{cir} is the mechanical degree of a whole circle that is 360 degrees.

The asymmetric flux barrier in AIPM machine is located near the rotor surface between the right side V-shape PM and the adjacent spoke PM in each pole, whose position is characterized by arc pitches from the central line of the flux barrier to the right side V-shape PM (θ_{abl}) and q -axis (θ_{abr}), respectively. To simplify the description of the flux barrier position, the position factor β_{pb} is defined as

$$\beta_{pb} = \theta_{abl} / \theta_{abr} \quad (2)$$

The dimensions of the flux barrier are described by the flux barrier width w_b and thickness h_b . θ_{ap} denotes the pole arc of V-shape PMs. Outer and inner radii of the rotor are R_{out} and R_{in} , respectively. b_{outv} , b_{inv} , b_{outs} , b_{ins} and b_{fb} are the iron bridge thicknesses of V-shape cavity, the spoke-type cavity and the flux barrier, respectively.

In general, the 1.5-layer mixed V-shape and spoke PM configuration employed in the symmetrical IPM-I machine uses V-shape PMs as the first layer and further employs spoke PMs to create a half layer structure to form multi-layer structure for torque enhancement while only using three pieces of PMs in each pole to avoid causing considerable increase of costs and difficulty in manufacturing. The 1.5-layer AIPM machine aims to achieve further increase of average torque by applying asymmetric features to utilize MFS effect with the same PMs as IPM-I machine.

B. Concept of MFS Technique

To briefly introduce the concept of MFS technique, a simple analytical model for both AIPM and conventional symmetrical IPM machines is established when magnetic saturation and cross-magnetization are neglected. The phasor diagram of stator current, flux linkage and PM flux linkage is shown in Fig. 3, where i_s , i_d , and i_q are the phasors of stator current and its components in d - and q -axes, respectively, ψ_d and ψ_q are the d - and q -axis flux linkages, respectively, ψ_{pm} , ψ_{pmd} and ψ_{pmq} are the PM flux linkage and its components in d - and q -axes, respectively, β is the current advancing angle as defined in (1), and α_s is the asymmetric angle in the AIPM machine.

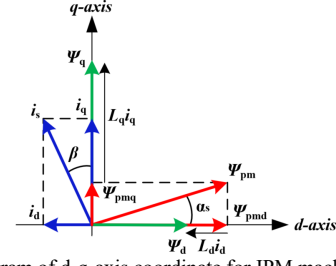


Fig. 3 Phasor diagram of d-q-axis coordinate for IPM machines.

$$\beta = \arctan\left(\frac{i_d}{i_q}\right) \quad (3)$$

The d - and q -axis flux linkages can be expressed by (4) and the general torque equation for IPM machines is given in (5).

$$\begin{cases} \psi_d = \psi_{pmd} - L_d i_d = \psi_{pm} \cos \alpha_s - L_d i_s \sin \beta \\ \psi_q = \psi_{pmq} + L_q i_q = \psi_{pm} \sin \alpha_s + L_q i_s \cos \beta \end{cases} \quad (4)$$

$$\begin{aligned} T_e &= \frac{3}{2} p (\psi_d i_d + \psi_q i_q) \\ &= \frac{3}{2} p \psi_{pm} i_s \cos(\beta - \alpha_s) + \frac{3}{4} p (L_q - L_d) i_s^2 \sin 2\beta \end{aligned} \quad (5)$$

where T_e is the combined output torque, and p is the number of pole pairs.

According to the torque production mechanism, the combined torque in IPM machines consists of two components: PM torque T_m produced by interaction between PM flux linkage and armature current and reluctance torque T_r due to rotor saliency, as shown in (6).

$$\begin{cases} T_m = \frac{3}{2} p \psi_{pm} i_s \cos(\beta - \alpha_s) \\ T_r = \frac{3}{4} p (L_q - L_d) i_s^2 \sin 2\beta \end{cases} \quad (6)$$

Thus, there is inherent current angle difference $\Delta\beta$ between current advancing angles for maximum PM and reluctance torque components, i.e. α_s and $\pi/4$, respectively. The current angle difference can be expressed as

$$\Delta\beta = \frac{\pi}{4} - \alpha_s \quad (7)$$

For conventional IPM machine, the asymmetric angle α_s remains 0 due to the symmetrical rotor geometry and the theoretical current angle difference is $\pi/4$. In AIPM machines, the peak points of PM and reluctance torque components are shifted closer with a positive α_s , thereby resulting in a notably smaller $\Delta\beta$ in AIPM machines compared with that of the conventional IPM machines due to utilizing MFS technique.

> REPLACE THIS LINE WITH YOUR PAPER IDENTIFICATION NUMBER (DOUBLE-CLICK HERE TO EDIT) <

4

Consequently, the maximum combined torque can increase significantly in AIPM machines without the enhancement of both maximum PM and reluctance torque components, which means that the torque enhancement of MFS technique does not require any extra PM usage.

III. DESIGN OPTIMIZATION

A. Global Parametric Optimization

To obtain optimal designs of all three machines with the same stator, rotor diameter and total PM usage, the global parametric optimization is carried out by using finite-element (FE) analysis and genetic algorithm (GA). To perform fair comparison between three machines with different rotor topologies, the same optimization conditions including the object and constraints are employed.

The object of design optimization is to maximize the maximum average torque at 10A and 1500 r/min when applying maximum torque per ampere (MTPA) method. Besides, two constraints are applied for optimization:

1) Torque ripple ratio $T_{ripple} < 20\%$ at maximum torque condition at 10A and 1500r/min. T_{ripple} is defined as

$$T_{ripple} = \frac{T_{p-p}}{T_{syn}} \times 100\% \quad (8)$$

where T_{p-p} and T_{syn} are peak-to-peak value of torque and average torque, respectively.

2) Three machines should have similar maximum von-Mises stress at 8000 r/min for similar mechanical robustness, which is revealed by using mechanical FE analysis.

In the optimization process, the same and fixed stator design and rotor diameter are employed for all three machines. The geometric variables are the design parameters of rotor except for outer and inner radii, as shown in Fig. 2. The main parameters of final optimal designs of three machines are shown in Table I.

TABLE I
MAIN DESIGN PARAMETERS OF FINAL OPTIMAL MACHINES

Parameters	Unit	AIPM	IPM-I	IPM-II
No of stator slots, N_s	-		24	
Pole pair number, p	-		2	
Stator winding	-	Single-layer three-phase distributed windings		
Number of turns per phase	-		480	
Air-gap length, δ	mm		1	
Stator outer radius, R_{so}	mm		50	
R_{rin}	mm		10	
R_{rout}	mm		26.9	
Core material	-		B50A600	
Total PM volume, V_{mag}	mm ³		12960	
PM material and grade	-		Nd-Fe-B, N38	
Remanence, B_r	T		1.23	
Rotor axial length, L_t	mm		50	
PM width, w_{pm}	mm	9	9	9
PM height, h_{pm}	mm	2.4	2.4	3.6

θ_{ap}	elec.deg.	87	90	110
β_{vs}	-	0.076	-	-
β_{pb}	-	0.088	-	-
w_b	mm	3.2	-	-
h_b	mm	2.0	-	-
b_{fb}	mm	0.5	-	-
b_{outv}	mm	0.5	0.5	0.6
b_{inv}	mm	0.6	0.6	0.7
b_{outs}	mm	0.5	0.5	-
b_{ins}	mm	0.5	0.5	-
b_{fb}	mm	0.5	-	-

B. Mechanical Stress

To achieve similar maximum mechanical stress in the design optimization of three final optimal machines and to confirm their mechanical robustness, the FE-based mechanical analysis is carried out at 8000 r/min for three machines. The mechanical characteristics of rotor materials are presented in Table II. In FE models, the boundary conditions between PMs and rotor core are set as non-linear frictional contacts.

TABLE II
MECHANICAL CHARACTERISTICS OF ROTOR MATERIALS

Characteristic	Unit	Rotor Core	Magnet
Young's modulus	Gpa	207	201
Density	kg/m ³	7700	7500
Tensile strength	Mpa	540	85
Yield strength	Mpa	380	350
Poisson's ratio	-	0.3	0.26

The FE-predicted von-Mises stress distributions in the rotor core of three machines are shown in Fig. 4. It shows that all three machines have similar maximum von-Mises stress and the maximum regions are all located on the junction rib between -V-shape PMs, although the maximum stress of conventional IPM-II machine is slightly higher than 1.5-layer IPM machines. Thus, the comparison confirms that optimal designs of three machines have similar mechanical strength at the same high-speed condition, thereby securing a fair comparison between the proposed AIPM machine, the proposed 1.5-layer IPM-I machine, and the conventional V-shape IPM-II benchmark machine by considering both electromagnetic and mechanical characteristics in the design optimization. Besides, as maximum von-Mises stress of three machines are significantly smaller than the yield strength of rotor core material at 8000 r/min, the mechanical design is robust.

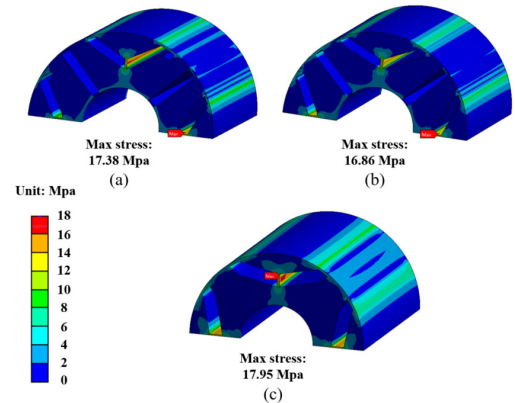


Fig. 4 von-Mises stress distributions on rotor cores at 8000 r/min. (a) AIPM. (b) IPM-I. (c) IPM-II.

> REPLACE THIS LINE WITH YOUR PAPER IDENTIFICATION NUMBER (DOUBLE-CLICK HERE TO EDIT) <

5

The mechanical stress distributions in PMs at 8000 r/min are shown in Fig. 5 to avoid the damage of brittle Nd-Fe-B magnets. As can be seen, the maximum stresses of three machines on PMs are notably smaller than the tensile strengths of PM material, which can ensure that the PMs will not rupture. Three machines show similar maximum stress on PMs and that of IPM-II machine is smaller than those of both 1.5-layer machines.

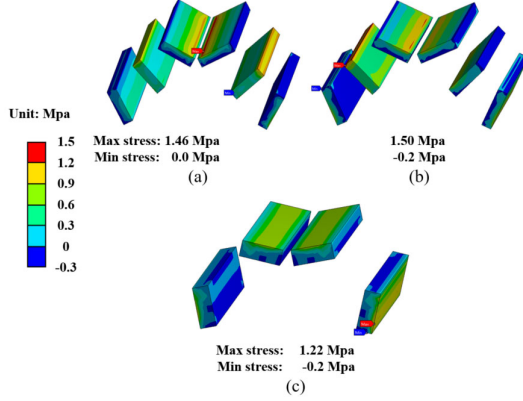


Fig. 5 Mechanical stress distributions on PMs at 8000 r/min. (a) AIPM. (b) IPM-I. (c) IPM-II.

IV. EFFECTS OF KEY ASYMMETRIC PARAMETERS IN AIPM MACHINE

This section investigates the influence of key design parameters of two asymmetric features in AIPM machine, namely, the asymmetry of V-shape PMs and the extra asymmetric flux barrier, on maximum average torque and open-circuit air-gap magnetic field. The maximum torque is obtained at 10A current and 1500 r/min when applying MTPA. In the investigation, optimal value of design parameters in Table I is used when parameters are not indicated.

A. Asymmetry of V-shape PMs

The influence of asymmetry in V-shape PMs in the AIPM machine (Table I), represented by an asymmetry factor β_{vs} , on maximum torque and open-circuit air-gap flux density is shown in Figs. 6 and 7, respectively. As revealed in Fig. 6 by both 2D- and 3D-FE analyses, a clear torque enhancement can only be achieved when asymmetric V-shape PMs and extra flux barriers are employed simultaneously. It is found that without flux barriers, the maximum torque decreases gradually with the increase of asymmetric factor. It is also found that optimal values for maximum torque exist for both optimal flux barrier and constant flux barrier designs for the AIPM machine, but the torque of optimal flux barrier design remains higher across the range of asymmetric factor. The influence of air-gap length on the effects of asymmetry of V-shape PMs is also compared in Fig. 6 with AIPM designs having 1 mm and 0.5 mm air-gap lengths, respectively. As can be seen, higher maximum torque can be achieved in the AIPM design with 0.5mm air-gap length in both 2D- and 3D-FE analyses. Further, using extra flux barrier can clearly increase the maximum torque, and optimal asymmetric factors exist for both optimal and constant flux barrier designs.

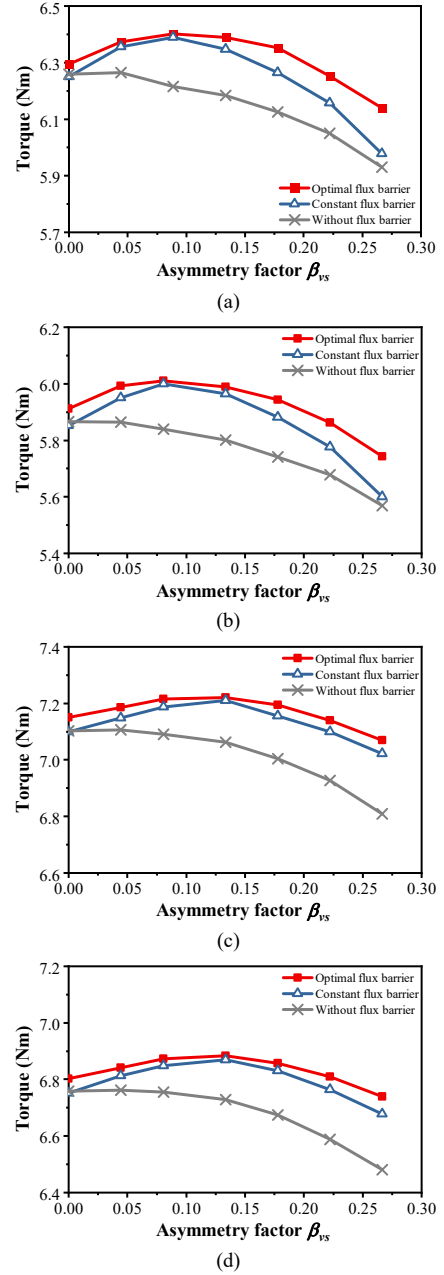


Fig. 6 Influence of asymmetry factor of V-shape PMs on maximum average torque using 2D- and 3D-FE analysis. The parameters of constant flux barrier are $w_b = 3.2$ mm and $h_b = 2.0$ mm. (a) Air-gap length $\delta=1$ mm, 2D-FE analysis. (b) Air-gap length $\delta=1$ mm, 3D-FE analysis. (c) Air-gap length $\delta=0.5$ mm, 2D-FE analysis. (d) Air-gap length $\delta=0.5$ mm, 3D-FE analysis.

To further reveal the influence of air-gap length on maximum torque and torque enhancement of both AIPM and IPM-I machines with 1.5-layer structure compared with the existing IPM-II machine, the maximum torques of three machine topologies with both 0.5 and 1mm air-gap length designs at 10A, 1500 r/min and MTPA are also compared using 2D- and 3D-FE analyses as shown in Table III. It shows that for all three machine topologies, the maximum torque increases with smaller air-gap length in both 2D- and 3D-FE analyses. It also reveals that compared with the IPM-II machine benchmark, the torque enhancement of the proposed AIPM and IPM-I machines remains for both 1mm and 0.5mm air-gap lengths, although as the air-gap length reduces, the torque increase ratios

> REPLACE THIS LINE WITH YOUR PAPER IDENTIFICATION NUMBER (DOUBLE-CLICK HERE TO EDIT) <

6

in the proposed AIPM and IPM-I machines become slightly smaller. The trends are similar in 2D-FE and 3D-FE analyses, although the maximum torques obtained by 3D-FE analysis are smaller than those calculated by 2D-FE analysis due to end-effect.

TABLE III
2D- AND 3D-FE PREDICTED MAXIMUM TORQUES WITH DIFFERENT AIR-GAPS

	Air-gap = 0.5 mm			Air-gap = 1.0 mm		
	AIPM	IPM-I	IPM-II	AIPM	IPM-I	IPM-II
Maximum torque, 2D/3D-FE (Nm)	7.22 /6.89	7.06 /6.74	6.74 /6.42	6.41 /6.01	6.26 /5.87	5.95 /5.57
Torque increase, 2D/3D-FE (%)	7.12 /7.23	4.72 /4.87	-	7.73 /7.89	5.71 /5.40	-

* Maximum torque is obtained at 10A current, 1500 r/min and MTPA.

As shown in Figs. 7 (a) and (b), the increase of asymmetric factor shifts the axis of open-circuit air-gap magnetic field gradually but shows negligible effect on shape of magnetic field and total harmonic distortion (THD). Fig. 7 (c) extracts the amplitude and angle shifting of fundamental component of air-gap flux density waveform, where angle shifting is the difference between phase angles of fundamental components in AIPM and IPM-I machines in each case. It also confirms that the increase of V-shape PMs asymmetry can increase the angle shifting gradually, with negligible reduction of the fundamental amplitude.

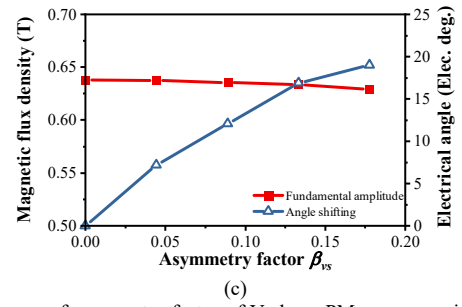
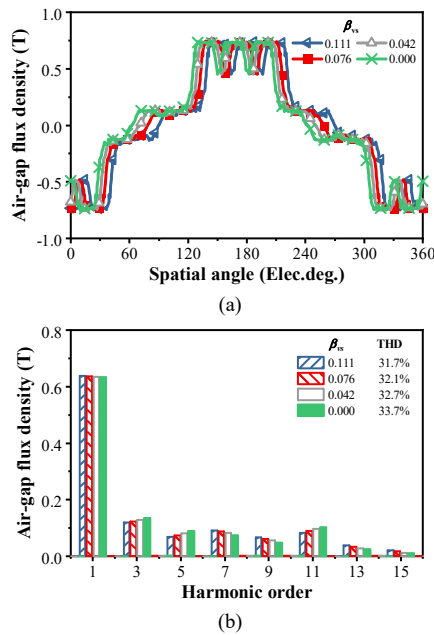


Fig. 7 Influence of asymmetry factor of V-shape PMs on open-circuit air-gap flux density when $w_b = 3.2$ mm and $h_b = 2.0$ mm. (a) Waveforms. (c) Spectra. (c) Amplitude and phase angle shifting of fundamental components.

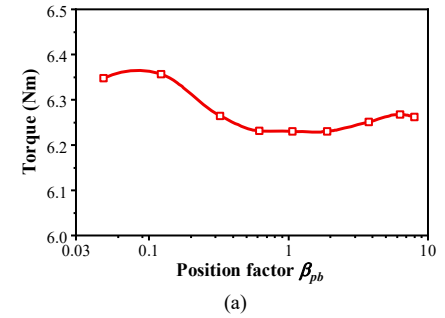


Fig. 8 Influence of flux barrier position. (a) Maximum torque at 10A current amplitude, (b) Open-circuit flux density waveforms with different flux barrier positions.

B. Position and Dimensions of Asymmetric Flux Barrier

The effect of the position of flux barrier, denoted by the position factor of flux barrier β_{pb} , is shown in Fig. 8. The position of flux barrier can clearly affect the maximum torque, but has no effect on open-circuit field. The trend of maximum torque via the position factor has two peak points, corresponding to designs when the flux barrier is geometrically near the V-shape PMs and the spoke PMs, respectively, while the optimal value exists when β_{pb} is small, i.e. flux barrier is close to the V-shape cavity. The influence of the dimensions of the flux barrier, i.e. the width and thickness, on maximum torque is shown in Fig. 9. Optimal values exist for both the width and thickness of flux barrier. Besides, both flux barrier dimensions have negligible effects on open-circuit field.

> REPLACE THIS LINE WITH YOUR PAPER IDENTIFICATION NUMBER (DOUBLE-CLICK HERE TO EDIT) <

7

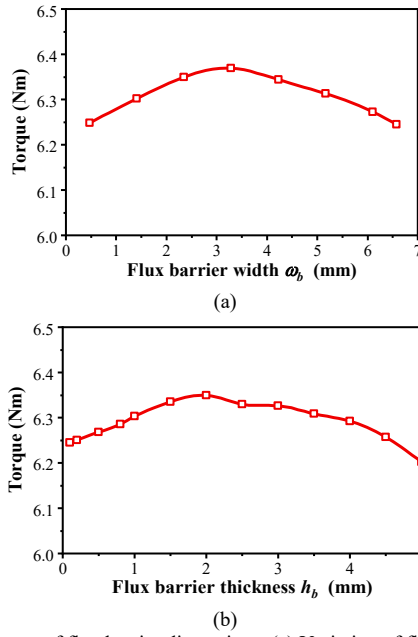


Fig. 9 Influences of flux barrier dimensions. (a) Variation of flux barrier width when $h_b = 2$ mm, (b) Variation of flux barrier thickness when $w_b = 2.8$ mm.

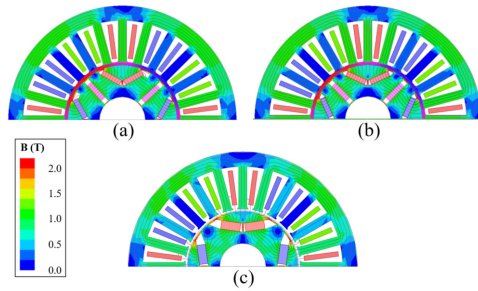


Fig. 10 Cross section, open-circuit magnetic flux density and flux line distribution of three final optimal machines. (a) AIPM, (b) IPM-I, (c) IPM-II.

V. ELECTROMAGNETIC PERFORMANCE COMPARISON

As the final optimal designs of three machines, i.e. the proposed AIPM and IPM-I machines with mixed V-shape and spoke-type PMs and the conventional V-shape IPM-II machine, are obtained in the previous study, electromagnetic performance of three machines are compared in this section to illustrate the merit and demerits of the proposed machine. The cross-sections and magnetic flux density and flux line distributions at open-circuit condition of three final optimal machines are shown in Fig. 10.

A. Open-circuit Characteristics

Fig. 11 compares the open-circuit air-gap flux density waveforms, spectra and fundamental components of three machines. All machines have similar amplitudes of fundamental flux densities, although the fundamental amplitude of conventional IPM-II is slightly smaller. AIPM machine has relatively higher harmonic distortion and its fundamental component waveform shows clear axis-shifting effect that indicates the MFS effect at open-circuit condition, compared with two symmetrical machines.

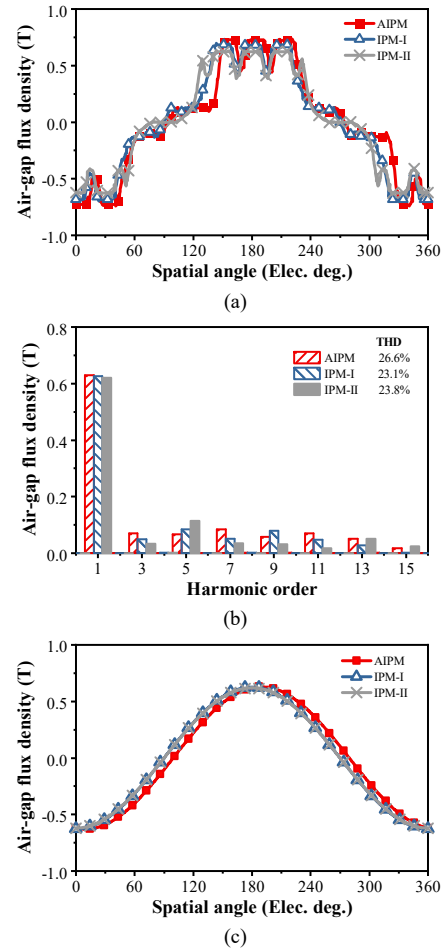


Fig. 11 Comparison of open-circuit air-gap flux densities. (a) Waveforms, (b) Spectra, (c) Waveforms of fundamental components.

The waveforms and spectra of open-circuit back electromotive force (EMF) of Phase A windings in three machines are compared in Fig. 12. The proposed AIPM machine has the highest amplitude of back EMF, followed by IPM-I, while IPM-II has the smallest, although their differences are small. Besides, the THDs of back EMF without the 3rd harmonics that are negligible in Y-connection windings in three machines are similar.

The waveforms and spectra of cogging torque in three machines are compared in Fig. 13. As can be seen, the proposed AIPM machine can significantly reduce the cogging torque compared with both the symmetrical IPM-I and -II machines, as the peak-to-peak value of cogging torque in the proposed AIPM machine is about 11.4% and 9.7% of that of IPM-I and IPM-II machines, respectively. It also reveals that the 12th harmonic is the dominant harmonic of cogging torques in all three machines.

> REPLACE THIS LINE WITH YOUR PAPER IDENTIFICATION NUMBER (DOUBLE-CLICK HERE TO EDIT) <

8

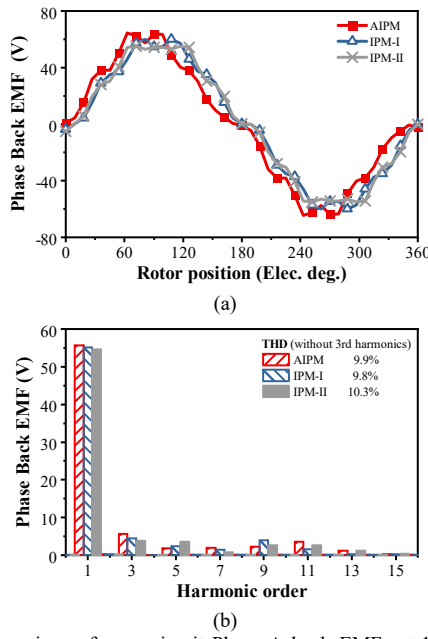


Fig. 12 Comparison of open-circuit Phase A back EMFs at 1500 r/min. (a) Waveforms, (b) Spectra.

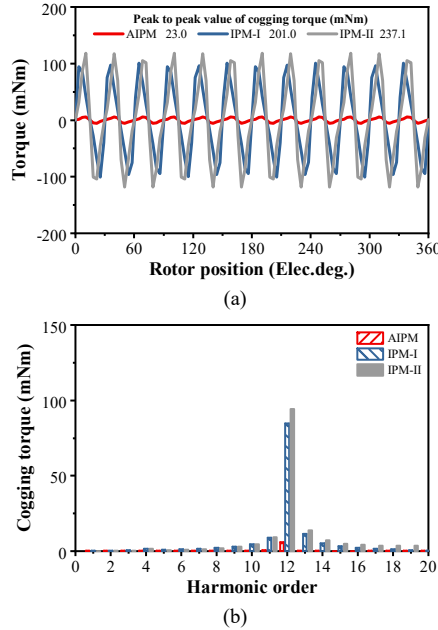


Fig. 13 Comparison of cogging torque. (a) Waveforms, (b) Spectra.

B. Torque Performance

Fig. 14 compares the average torque and torque components versus current advancing angle of three machines at 10A and 1500 r/min. The highest maximum torque is achieved in AIPM machine, followed by 1.5-layer structure IPM-I, and IPM-II has the smallest value. It can be observed that AIPM reaches the 0Nm average torque at a higher current angle compared with other machines, which indicates the MFS effect on average torque performance.

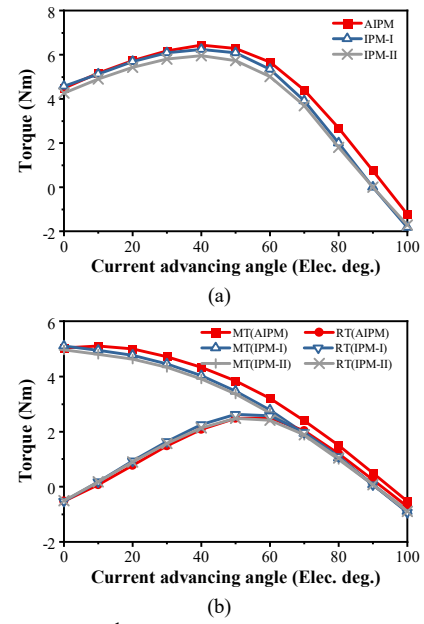


Fig. 14 Average torque and torque components versus current advancing angle at 10A and 1500 r/min. (a) Average torque, (b) Torque components.

To reveal the torque enhancement in both 1.5-layer machines, torque components of three machines are extracted using frozen permeability methods [24] as shown in Fig. 14 (b), in which MT and RT denote PM and reluctance torque components, respectively. Key torque performances are also given in Table IV. The 1.5-layer symmetrical IPM-I machine has larger maximum PM and reluctance torque and similar $\Delta\beta$ compared with the conventional V-shape IPM-II machine. Therefore, IPM-I machine achieves a 5.7% increase of maximum torque due to the 1.5-layer configuration. The proposed AIPM machine employs asymmetric features in the rotor design, compared with symmetrical 1.5-layer IPM-I machine. The PM torque of AIPM machine reaches the peak point when current angle is about 10 Elec. deg while maximum PM torque points of two symmetrical machines are at 0 Elec. deg. Besides, maximum reluctance torque of three topologies are achieved at similar current angles. Consequently, significant reduction of current angle difference between maximum PM and reluctance torque components is achieved in AIPM machine, as denoted by the smaller $\Delta\beta$ in AIPM machine in Table IV. Although the increase of T_r^A in IPM-I machine diminishes in AIPM machine due to asymmetric rotor structure compared with conventional IPM-II machine, AIPM machine has similar PM torque amplitude to IPM-I and a significantly smaller $\Delta\beta$, which results in further torque enhancement in AIPM machine without introducing any extra costs because the same PMs are employed and only difference is the design of rotor core lamination. Thus, it is demonstrated that the torque enhancement in AIPM machine benefits from both the 1.5-layer structure and MFS effect, and the 1.5-layer PM configuration can also provide the increase of maximum average torque effectively when employed individually. Moreover, it can also be observed that the PM torque components of IPM-I and IPM-II machines reaching zero at about 90 elec. deg., while that of the AIPM machine reaching zero at approximately 94 elec. deg. as the other result of utilizing MFS effect in asymmetric rotor

> REPLACE THIS LINE WITH YOUR PAPER IDENTIFICATION NUMBER (DOUBLE-CLICK HERE TO EDIT) <

9

structure, which shifts the torque-angle characteristics of PM torque components towards higher current advancing angle.

TABLE IV

KEY TORQUE PERFORMANCE OF THREE TOPOLOGIES

Performance	Unit	AIPM	IPM-I	IPM-II
T_{syn}^A	Nm	6.41	6.26	5.95
T_m^A	Nm	5.11	5.10	4.96
T_r^A	Nm	2.50	2.63	2.48
$\Delta\beta$	Elec. deg.	46	52	54
TE	%	7.73	5.71	-

* T_{syn}^A , T_m^A , T_r^A are amplitudes of average torque, PM torque and reluctance torque, respectively; $\Delta\beta$ is the current angle difference between maximum PM and reluctance torque; TE is the torque enhancement ratio of topologies comparing with IPM benchmark; all at 1500 r/min and 10 A current amplitude.

Fig. 15 compares the maximum average torques at different current in three machines. It reveals that approximately 8% and 6% increases of torque can be achieved in AIPM and IPM-I machines, respectively, across the whole range of current, compared with the IPM-II benchmark machine. Fig. 16 compares torque waveforms at maximum torque conditions at 10 A and 1500 r/min in three machines. It confirms that three machines show torque ripple smaller than 20%, as required in the design optimization. It is also found that the torque ripple of IPM-I machine is clearly smaller than AIPM and IPM-II machines. The magnetic flux density and flux line distributions of three machines at the maximum torque conditions in Fig. 16 at 10 A and 1500 r/min are illustrated in Fig. 17.

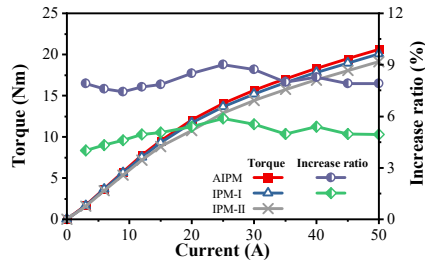


Fig. 15 Average torque versus current at 1500 r/min when applying MTPA.

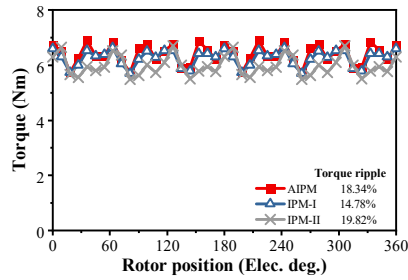


Fig. 16 Comparison of torque waveforms at 10A, 1500 r/min and MTPA.

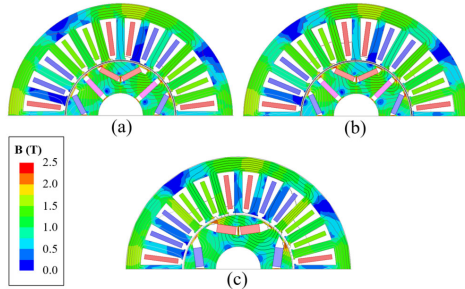


Fig. 17 On-load field and flux line distributions of machines at 10A, 1500 r/min and MTPA. (a) AIPM. (b) IPM-I. (c) IPM-II.

TABLE V
EFFECTS OF ROTATION DIRECTIONS AND MODES ON MAXIMUM TORQUE
(UNIT: NM)

Machines	Anti-clockwise direction		Clockwise direction	
	Motor mode	Generator mode	Motor mode	Generator mode
AIPM	6.41	6.28	6.28	6.41
IPM-I	6.26	6.26	6.26	6.26
IPM-II	5.95	5.95	5.95	5.95

The influences of rotation direction and operation mode on maximum torque of AIPM and IPM machines at 10A and 1500 r/min are compared as shown in Table V. The anti-clockwise direction is the reference rotation direction of machines in this paper using the stator winding configuration illustrated in Fig. 1. For the reversed clockwise rotation direction, the winding phase sequences are changed to ensure stable torque production. The comparison shows clear effects of rotation direction and operation mode on maximum torque in AIPM machine, while the influence in symmetrical IPM machine is negligible. AIPM machine has smaller maximum torque in the generator mode compared with that in the motor mode in the anti-clockwise direction, but the maximum torque is higher in generator mode than that in motor mode with clockwise direction rotation. Moreover, albeit with the influence of rotation direction and operation mode, the proposed AIPM machine shows the highest maximum torque at all conditions compared with the IPM-I and IPM-II machines.

C. CPSR Performance and Efficiency Maps

To compare the CPSR performance of three machines, the torque-speed and power-speed curves are obtained based on the method provided in [25]-[26] and MTPA is employed to fully utilize the torque capability. The torque- and power-speed curves at maximum current 10A and DC bus voltage 120V are compared in Fig. 18.

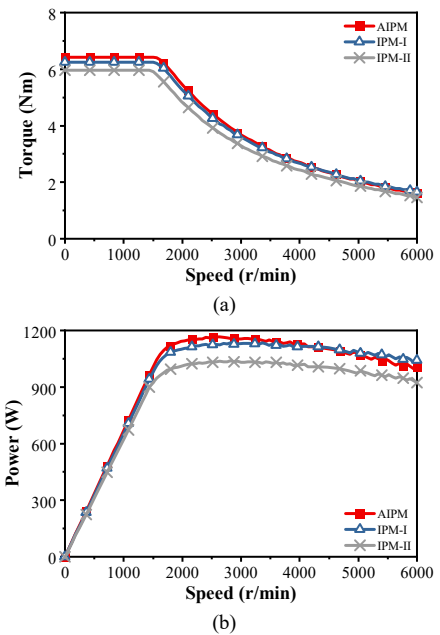


Fig. 18 Comparison of CPSR performances at DC bus voltage U_{dc} 120V, maximum current 10A and MTPA. (a) Torque-speed curve. (b) Power-speed curve.

> REPLACE THIS LINE WITH YOUR PAPER IDENTIFICATION NUMBER (DOUBLE-CLICK HERE TO EDIT) <

10

Both AIPM and IPM-I machines show clear increase of torque and power across the whole speed range compared with the conventional IPM-II. AIPM machine shows higher torque/power in the constant-torque region and the merit remains in the constant-power region when the speed is smaller than 4000 r/min, compared with the symmetrical 1.5-layer IPM-I machine. However, with further increase of speed, the torque/power enhancement of AIPM machine diminishes compared with IPM-I machine.

The efficiency maps of three machines are also obtained as shown in Fig. 19. In general, the AIPM machine shows the largest high efficiency regions compared with IPM-I and IPM-II machines, in particular at high torque conditions due to the torque enhancement. The IPM-I machine also has higher efficiency compared with the conventional IPM-II machine. Besides, Both AIPM and IPM-I machines using the 1.5-layer configuration can achieve higher efficiency at high-speed conditions compared the conventional V-shape IPM-II machine.

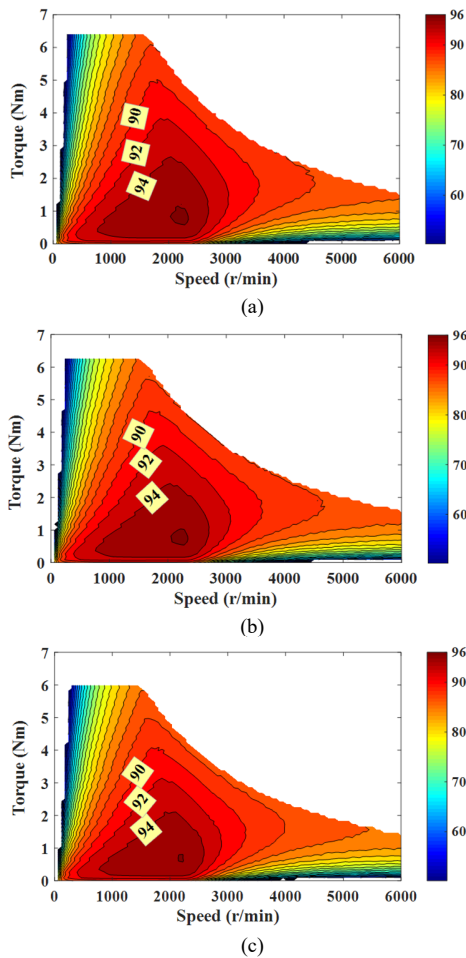


Fig. 19 Efficiency maps at maximum current 10A, U_{dc} 120V and MTPA. (a) AIPM. (b) IPM-I. (c) IPM-II.

VI. EXPERIMENTAL VALIDATION

The proposed AIPM machine shown in Table I has been prototyped to verify the simulated performance based on FE analysis. The photos of rotor and stator of the prototype and their laminations are shown in Figs. 20 (a) and (b), respectively, while the photo of the prototype test platform is shown in Fig.

20 (c).

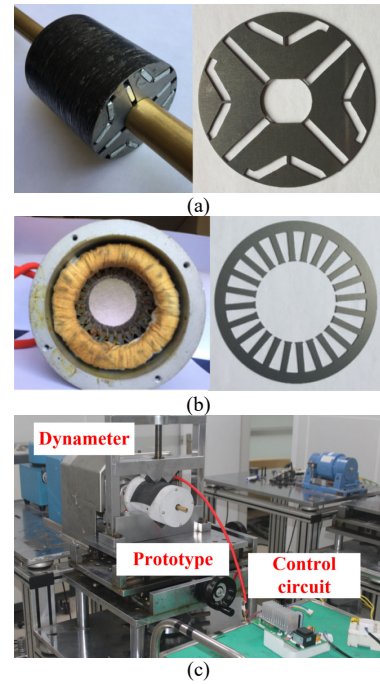


Fig. 20 Photos of prototypes and test rig. (a) Rotor and the lamination. (b) Stator and the lamination. (c) The test rig.

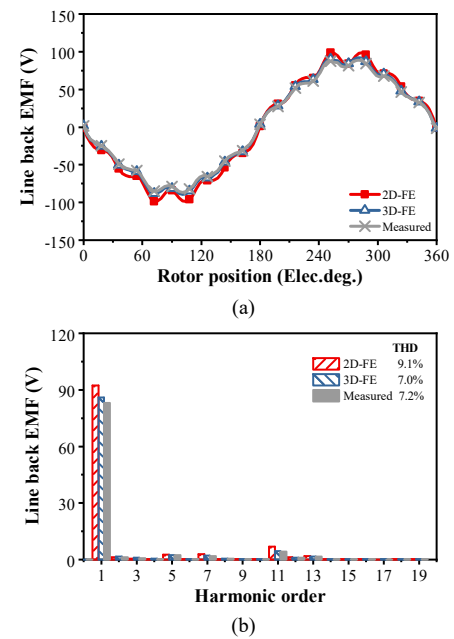


Fig. 21 Line back EMF of the prototype at 1500 r/min. (a) Waveforms. (b) Spectra.

The measured and FE-predicted line back EMF waveforms at 1500 r/min are compared in Fig. 18 (a), and the spectra of waveforms are compared in Fig. 18 (b). It shows that the predicted line back EMF obtained by 3D-FE analysis matches well with the measured one. There is relatively higher error in 2D FE-predicted results compared with that in 3D FE-predicted results due to neglect of end-region effect in 2D FE analysis.

The FE-predicted and measured waveforms of cogging torque in the prototype are compared in Fig. 22. It confirms the advantages of low cogging torque in the proposed AIPM machine.

> REPLACE THIS LINE WITH YOUR PAPER IDENTIFICATION NUMBER (DOUBLE-CLICK HERE TO EDIT) <

11

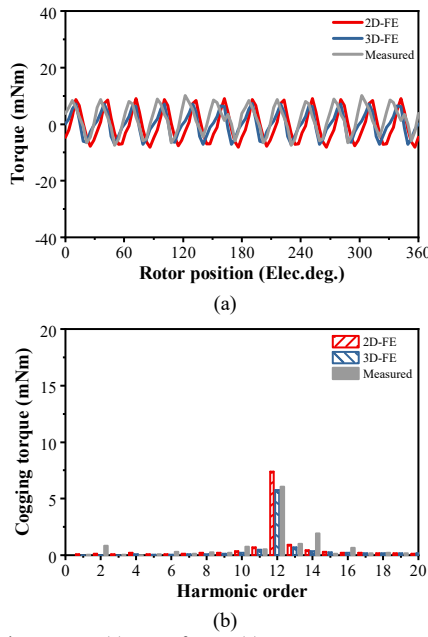


Fig. 22 Cogging torque. (a) Waveforms. (c) Spectra.

To measure static torques of the prototype versus rotor position, dc currents are injected into three-phase stator windings when rotating the rotor step by step and the current configuration of stator windings remain $I_A = I_p$ and $I_B = I_C = -I_p/2$ during the test, where I_p is the dc current. Static torque waveforms are compared in Fig. 23. It shows good agreement between measured and FE-predicted results in particular the 3D-FE analysis results.

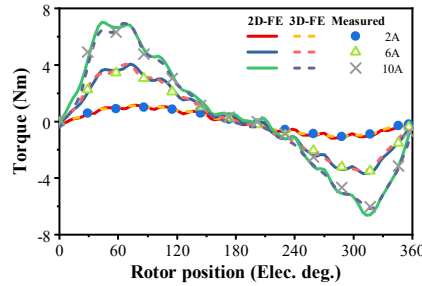


Fig. 23 Static torque with different current amplitude I_p .

The comparison of torque/power-speed curves between FE-predicted and measured results is provided in Fig. 24. The torque- and power-speed curves in Figs. 24 (a) and (b) of the prototype are tested by using the dynamometer with 120V dc bus voltage, maximum current amplitude 6A, and speed range 500-3000 r/min due to the limitation of the test rig. The d - and q -axis currents used in FE analysis simulation and experiments are shown in Fig. 20 (c).

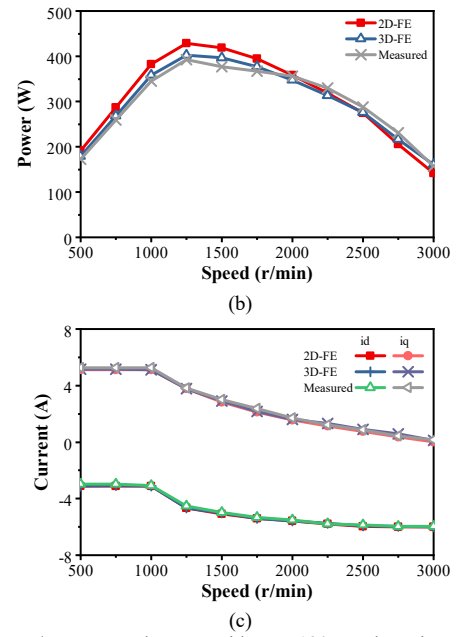
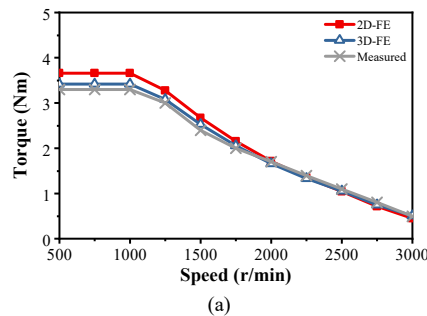
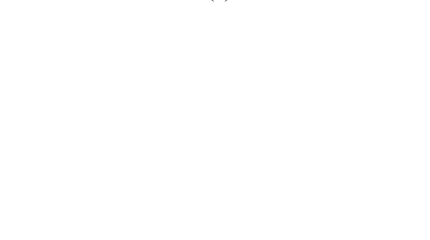
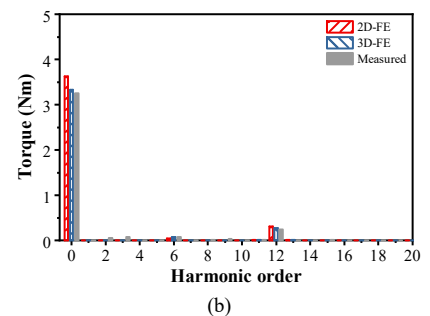
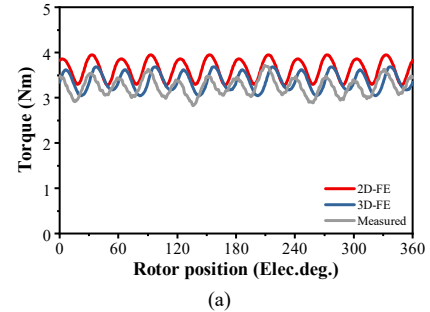


Fig. 24 Torque/power-speed curves with $U_{dc}=120V$ and maximum current 6A. (a) Torque-speed curve. (b) Power-speed curve. (c) d - and q -axis currents.

The waveforms and spectra of FE-predicted and measured dynamic torque waveforms at 6A current and MTPA are shown in Figs. 25 (a) and (b), respectively. In Fig. 25 (c), the predicted maximum average torque across 0-6 A current range at 1500 r/min and MTPA using 2D and 3D FE analysis are compared with the measured results. It also reveals the good agreement between 3D-FE analysis and measured results and relatively higher error in 2D-FE analysis results.



> REPLACE THIS LINE WITH YOUR PAPER IDENTIFICATION NUMBER (DOUBLE-CLICK HERE TO EDIT) <

12

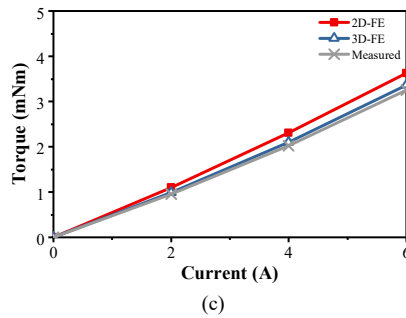


Fig. 25 Dynamic experiment results. (a) Torque waveforms at 6A current and MTPA. (b) Spectra of torque waveforms. (c) Maximum average torque versus current.

VII. CONCLUSION

In this paper, a novel AIPM rotor topology featured by the asymmetric 1.5-layer mixed V-shape and spoke PM structure and asymmetric flux barrier in each pole is proposed for torque enhancement in IPM synchronous machine. As spoke PMs are employed, the simple 1.5-layer PM configuration is used in both proposed AIPM and IPM-I machines with only three pieces of PMs in each pole. The 1.5-layer AIPM and IPM machines have significant torque enhancement compared with the single-layer V-shape benchmark IPM-II machine using the same stator, rotor diameter and total PM volume, while AIPM machine can achieve further increase of average torque compared with the symmetrical 1.5-layer IPM-I machine without any extra costs. The comparison between the proposed AIPM, IPM-I and the IPM-II benchmark machines using FE analysis confirms that the torque enhancement in AIPM machine is due to both the 1.5-layer PM configuration and MFS effect. Moreover, other advantages of AIPM machine including significant reduction of cogging torque and improvement of efficiency are revealed. The proposed AIPM machine also shows good CPSR performance. The measured results of the AIPM prototype are provided to validate the FE analyses.

REFERENCES

- [1] Z. Zhu, W. Chu, and Y. Guan, "Quantitative comparison of electromagnetic performance of electrical machines for HEVs/EVs," *CES Trans. on Electr. Mach. and Syst.*, vol. 1, no. 1, pp. 37-47, Jul. 2017.
- [2] Z. Zhu and D. Howe, "Electrical machines and drives for electric, hybrid, and fuel cell vehicles," *Proc. IEEE*, vol. 95, no. 4, pp. 746-765, Apr. 2007.
- [3] K. Chau, C. C. Chan, and C. Liu, "Overview of permanent-magnet brushless drives for electric and hybrid electric vehicles," *IEEE Trans. Ind. Electron.*, vol. 55, no. 6, pp. 2246-2257, May 2008.
- [4] X. Liu, H. Chen, J. Zhao, and A. Belahcen, "Research on the performances and parameters of interior PMSM used for electric vehicles," *IEEE Trans. Ind. Electron.*, vol. 63, no. 6, pp. 3533-3545, Jun. 2016.
- [5] K. Kamiev, J. Montonen, M. P. Ragavendra, J. Pyrhönen, J. A. Tapia, and M. Niemelä, "Design principles of permanent magnet synchronous machines for parallel hybrid or traction applications," *IEEE Trans. Ind. Electron.*, vol. 60, no. 11, pp. 4881-4890, Nov. 2013.
- [6] R. Dutta, A. Pouramin, and M. F. Rahman, "A novel rotor topology for high-performance fractional slot concentrated winding interior permanent magnet machine," *IEEE Trans. Energy Convers.*, vol. 36, no. 2, pp. 658-670, June 2021.
- [7] Y. Honda, T. Higaki, S. Morimoto, and Y. Takeda, "Rotor design optimisation of a multi-layer interior permanent-magnet synchronous motor," *IEE Proc. - Electr. Power Appl.*, vol. 145, no. 2, pp. 119-124, Mar. 1998.
- [8] Y. Hu, S. Zhu, C. Liu, and K. Wang, "Electromagnetic performance analysis of interior PM machines for electric vehicle applications," *IEEE Trans. Energy Convers.*, vol. 33, no. 1, pp. 199-208, Mar. 2018.
- [9] S. Zhu, W. Chen, M. Xie, C. Liu, and K. Wang, "Electromagnetic performance comparison of multi-layered interior permanent magnet machines for EV traction applications," *IEEE Trans. Magn.*, vol. 54, no. 11, pp. 1-5, Nov. 2018.
- [10] S. Ooi, S. Morimoto, M. Sanada, and Y. Inoue, "Performance evaluation of a high-power-density PMASynRM with ferrite magnets," *IEEE Trans. Ind. Appl.*, vol. 49, no. 3, pp. 1308-1315, May-Jun., 2013.
- [11] M. Obata, S. Morimoto, M. Sanada, and Y. Inoue, "Performance of PMASynRM with ferrite magnets for EV/HEV applications considering productivity," *IEEE Trans. Ind. Appl.*, vol. 50, no. 4, pp. 2427-2435, Jul.-Aug. 2014.
- [12] H. Cai, B. Guan, and L. Xu, "Low-cost ferrite PM-assisted synchronous reluctance machine for electric vehicles," *IEEE Trans. Ind. Electron.*, vol. 61, no. 10, pp. 5741-5748, Oct. 2014.
- [13] S. S. Maroufian and P. Pillay, "Design and analysis of a novel PM-assisted synchronous reluctance machine topology with AlNiCo magnets," *IEEE Trans. on Ind. Appl.*, vol. 55, no. 5, pp. 4733-4742, Sep.-Oct. 2019.
- [14] X. Zeng, L. Quan, X. Zhu, L. Xu, and F. Liu, "Investigation of an asymmetrical rotor hybrid permanent magnet motor for approaching maximum output torque," *IEEE Trans. Appl. Supercond.*, vol. 29, no. 2, pp. 1-4, Jan. 2019.
- [15] G. Liu, G. Xu, W. Zhao, X. Du, and Q. Chen, "Improvement of torque capability of permanent-magnet motor by using hybrid rotor configuration," *IEEE Trans. Energy Convers.*, vol. 32, no. 3, pp. 953-962, Feb. 2017.
- [16] W. Zhao, F. Zhao, T. A. Lipo, and B. I. Kwon, "Optimal design of a novel V-type interior permanent magnet motor with assisted barriers for the improvement of torque characteristics," *IEEE Trans. Magn.*, vol. 50, no. 11, pp. 1-4, Dec. 2014.
- [17] Y. Xiao, Z. Q. Zhu, G. W. Jewell, J. Chen, D. Wu, and L. Gong, "A novel spoke-type asymmetric rotor interior permanent magnet machine," *IEEE Trans. Ind. Appl.*, vol. 57, no. 5, pp. 4840-4851, Sept.-Oct. 2021.
- [18] F. Xing, W. Zhao, and B. I. Kwon, "Design and optimisation of a novel asymmetric rotor structure for a PM-assisted synchronous reluctance machine," *IET Electr. Power Appl.*, vol. 13, no. 5, pp. 573-580, May 2018.
- [19] H. Yang, C. Qian, W. Wang, H. Lin, Z. Q. Zhu, S. Niu, W. Liu and S. Lyu, "A novel asymmetric-magnetic-pole interior PM machine with magnet-axis-shifting effect," *IEEE Trans. Ind. Appl.*, early access.
- [20] Y. Xiao, Z. Q. Zhu, G. W. Jewell, J. Chen, D. Wu, and L. Gong, "A novel asymmetric interior permanent magnet machine for electric vehicles," *IEEE Trans. Energy Convers.*, vol. 36, no. 3, pp. 2404-2415, Sept. 2021.
- [21] Y. Xiao, Z. Q. Zhu, G. W. Jewell, J. Chen, D. Wu, and L. Gong, "A novel asymmetric rotor interior permanent magnet machine with hybrid-layer permanent magnets," *IEEE Trans. on Ind. Appl.*, early access.
- [22] W. Chai, H. -M. Yang, F. Xing and B. -i. Kwon, "Analysis and design of a PM-assisted wound rotor synchronous machine with reluctance torque enhancement," *IEEE Trans. Ind. Electron.*, vol. 68, no. 4, pp. 2887-2897, Apr. 2021.
- [23] Y. Xiao, Z. Q. Zhu, J. T. Chen, D. Wu, and L. M. Gong, "A novel interior permanent magnet synchronous machine," *2020 Int. Conf. on Electric Mach. (ICEM)*, Gothenburg, Sweden, 2020.
- [24] Z. Q. Zhu and W. Q. Chu, "Advanced frozen permeability technique and applications in developing high performance electrical machines," *Trans. of China Electrotech. Soc.*, vol. 31, no. 29, pp. 13-29, Oct. 2016.
- [25] G. Qi, J. T. Chen, Z. Q. Zhu, D. Howe, L. B. Zhou and C. L. Gu, "Influence of skew and cross-coupling on flux-weakening Performance of permanent-magnet brushless AC machines," *IEEE Trans. Magn.*, vol. 45, no. 5, pp. 2110-2117, 2009.
- [26] W. Q. Chu, Z. Q. Zhu, J. Zhang, X. Liu, D. A. Stone, and M. P. Foster, "Investigation on Operational Envelops and Efficiency Maps of Electrically Excited Machines for Electrical Vehicle Applications," *IEEE Trans. Magn.*, vol. 51, no. 4, pp. 1-10, Apr. 2015.

> REPLACE THIS LINE WITH YOUR PAPER IDENTIFICATION NUMBER (DOUBLE-CLICK HERE TO EDIT) <

13



Y. Xiao received the B. Eng. and Ph. D. degrees in electrical engineering from Huazhong university of Science and Technology, Wuhan, China, in 2013 and 2018, respectively. Since 2018, he has been working towards his second Ph.D. degree in electronic and electrical engineering with the University of Sheffield, U.K. His current research interests include the design of permanent magnet machines.



L.M. Gong received the B.Eng. and M.Sc. degrees in electrical engineering from the Huazhong University of Science and Technology, Wuhan, China, in 2001 and 2004, respectively, and the Ph.D. degree in electrical and electronic engineering from the University of Sheffield, Sheffield, U.K., in 2012. Since 2012, he has been with the Midea Welling Motor Technology (Shanghai) Co., Ltd., Shanghai. He is currently General Manager of Servotronics Motion Control Company, Midea Group. His research interests include control of permanent-magnet brushless machines and power electronics.



Z.Q. Zhu (M'90–SM'00–F'09) received the B.Eng. and M.Sc. degrees from Zhejiang University, Hangzhou, China, in 1982 and 1984, respectively, and the Ph.D. degree from The University of Sheffield, Sheffield, U.K., in 1991, all in electrical and electronic engineering. Since 1988, he has been with The University of Sheffield, where he is currently a Professor with the Department of Electronic and Electrical Engineering, the Head of the Electrical Machines and Drives Research Group, the Royal

Academy of Engineering/Siemens Research Chair, the Academic Director of Sheffield Siemens Gamesa Renewable Energy Research Centre, the Director of Midea Electrical Machines and Control Systems Research Centres, and the Director of Sheffield CRRC Electric Drives Technology Research Centre. His current major research interests include the design and control of permanent-magnet brushless machines and drives for applications ranging from electrified transportation through domestic appliance to renewable energy. He is the recipient of 2019 IEEE Industry Applications Society Outstanding Achievement Award and the 2021 IEEE Nikola Tesla Award. He is a Fellow of the Royal Academy of Engineering and the IET, UK.



G. W. Jewell received the B.Eng. and Ph.D. degrees in electrical engineering from The University of Sheffield, Sheffield, U.K., in 1988 and 1992, respectively. Since 1994, he has been a Member of Academic Staff with the Department of Electronic and Electrical Engineering, The University of Sheffield, where he is currently a Professor of Electrical Engineering, the Head of the Department, and the Director of the Rolls-Royce University Technology Centre in Advanced Electrical Machines. He held an

Engineering and Physical Sciences Research Council Advanced Research Fellowship from 2000 to 2005 and a Royal Society Industry Fellowship with Rolls-Royce from 2006 to 2008. His research interests include the modeling and design of a wide variety of electromagnetic devices, notably electrical machines for aerospace and high-temperature applications.



J. T. Chen (M'09–SM'13) received the B.Eng. and M.Sc. degrees from Huazhong University of Science and Technology, Wuhan, China, in 2001 and 2004, respectively, and the Ph.D. degree from The University of Sheffield, Sheffield, U.K., in 2009, all in electrical engineering. From 2004 to 2006, he was an Engineer with Delta Electronics (Shanghai) Company, Ltd., Shanghai, China. He is currently a General Manager of Midea Automotive Components Ltd and also with the Midea Shanghai Motors and Drives

Research Center, Shanghai, China. His major research interests include the design of permanent magnet machines.



D. Wu received the M.Sc. degree in electrical engineering from the Huazhong University of Science and Technology, Wuhan, China, in 2011, and the Ph.D. degree in electronic and electrical engineering from the University of Sheffield, Sheffield, U.K., in 2015. Since 2011, he has been working with the Midea Welling Motor Technology (Shanghai) Co., Ltd., Shanghai, China, and is currently Head of Motor Development Department, Welling, Midea Group. His major research interests include the design and analysis of permanent-magnet brushless machines.